
Proceedings Paper:
Kana Padinharu, D.K., Li, G.-J. orcid.org/0000-0002-5956-4033, Zhu, Z.Q. et al. (3 more authors) (2020) Effect of airgap length on electromagnetic performance of surface mounted permanent magnet Vernier machine. In: Proceedings of 2020 International Conference on Electrical Machines (ICEM). 2020 International Conference on Electrical Machines (ICEM), 23-26 Aug 2020, Online conference. IEEE , pp. 1882-1888. ISBN 9781728199467

https://doi.org/10.1109/ICEM49940.2020.9270829

Effect of Airgap Length on Electromagnetic Performance of Surface Mounted Permanent Magnet Vernier Machine

D. K. Kana Padinharu, G. J. Li, Z. Q. Zhu, Z. Azar, R. Clark, and A. Thomas

***Abstract* – This paper investigates the effect of airgap length on the electromagnetic performance of 3kW surface mounted permanent magnet Vernier (SPM-V) machine. The performance is compared with a conventional surface mounted permanent magnet (SPM) machine with same airgap length using 2D Finite Element Analysis (2D FEA). For each airgap length, the slot/pole number combination for the SPM-V machine is investigated to achieve the optimal performance compared to the conventional SPM machine. The results show that the SPM-V machine can achieve much higher torque capability than the conventional SPM machine at smaller airgap length. However, there is an optimal airgap length beyond which the torque performance of SPM-V machines drops below the conventional SPM counterparts. Moreover, unlike the conventional SPM machines, the power factor of SPM-V machines drops significantly with increase in airgap length.**

***Index Terms*—Airgap permeance, leakage flux, power factor, Vernier machine.**

I. Introduction

Direct drive machines are gaining popularity in applications such as electric vehicle [1], [2], offshore-wind power generation [3], [4], etc. Direct drive technology makes the drivetrain system much simpler and reliable by eliminating the requirement of gearboxes or any mechanical transmission between the machine and the load. Most of the direct drive applications usually adopt a permanent magnet machine with an outer rotor topology [1], [5], [6]. This makes it convenient to mount the rotor directly to the hub and also favorable to realize large number of poles required for low operating speed [7]. However, the large size of direct drive machines due to their low operating speed makes these machines very bulky and costly [8]. Different permanent magnet machine topologies have been proposed in the past to reduce the size and weight of direct drive machines such as transverse flux machines [9], axial field machines [7], [10], [11] and magnetically geared machines [12], [13]. However, these proposed machines either have a complex 3D structure or have multiple airgaps which makes them difficult to manufacture.

In the recent decade, Vernier machines have become very popular because of their simple structure (similar to conventional SPM machines) and high torque density. Vernier machines work on the principle of flux modulation/magnetic gearing principle which makes them inherently favorable for direct drive multi-pole structure. Different direct drive Vernier machines have been proposed in literature to improve their torque density. A 2.2kW outer rotor permanent magnet Vernier machine with split teeth stator has been proposed in [14] for direct drive wind power generation. The design adopts an airgap length of 0.6mm at 150rpm with machine outer diameter of 233mm. Similarly, an outer rotor Vernier machine with magnets on both sides of the rotor and the stator is discussed in [15] for in-wheel motor application. This machine is designed with 2mm airgap length for a 180mm machine outer diameter (150rpm speed). A linear Vernier machine with a modular structure having 1.5mm airgap length has been proposed in [16] to minimize force ripple for direct drive servo applications. In general, the above mentioned references discuss the high torque density capability of Vernier machines for different direct drive applications. It is also noted that Vernier machines with similar outer diameters can be designed with different airgap lengths according to the specific applications and design requirements. This calls for a systematic study of the performance of SPM-V machine for different airgap lengths, which has not been reported in literature.

This paper will compare the SPM-V machine with the conventional SPM machine for different airgap lengths. Different slot/pole number combinations have been considered for the SPM-V machine to analyze the inter-pole leakage effect with increasing pole number and airgap length. An outer rotor topology, for example, the schematic shown in Fig. 1, will be considered for this study as it is more favorable for direct drive applications.

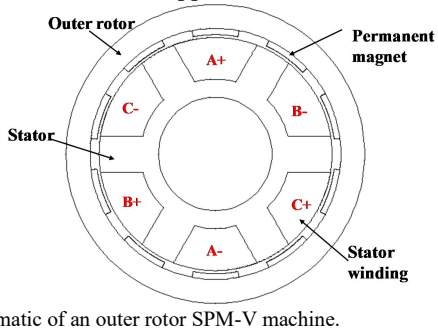

Fig. 1. Schematic of an outer rotor SPM-V machine.

II. Working Principle of SPM-V Machine and Importance of Airgap Permeance

As mentioned previously, SPM-V machines work on the principle of airgap flux modulation. This can be explained as follows. The large open stator slots in SPM-V machine shown in Fig. 1 create an airgap permeance (Λ) given by [17]

This work is supported by the UK EPSRC Prosperity Partnership "A New Partnership in Offshore Wind" under Grant No. EP/R004900/1.

D. K. Kana Padinharu, G. J. Li and Z. Q. Zhu are with the Department of Electronic & Electrical Engineering, The University of Sheiffield, U.K, (e-mail: dkkanapadinharu1@sheffield.ac.uk, g.li@sheffield.ac.uk and z.q.zhu@sheffield.ac.uk).

Z. Azar, R. Clark and A. Thomas are with Siemens Gamesa Renewable Energy Limited, U.K, (email: ziad.azar@siemensgamesa.com, richard.clark@siemensgamesa.com, arwyn.thomas@siemensgamesa.com

$$\Lambda(\theta_s) = \Lambda_0 + \sum_{J=1,2,3\ldots}^{\infty} \Lambda_j \cos(jZ\theta_s) \quad (1)$$

where Z is the number of stator slots, Λ_0 is the DC component of airgap permeance and Λ_j is the magnitude of the j^{th} order harmonic of permeance function. The MMF (F_{PM}) produced by permanent magnets is given by [18]

$$F_{PM}(\theta_s, t) = \sum_{i=1,3,5\ldots}^{\infty} F_{PMi} \cos(iP_r\theta_s - i\omega_e t) \quad (2)$$

where P_r is the rotor pole pair number, ω_e is the electrical angular velocity, F_{PMi} is the amplitude of the i^{th} order MMF harmonic and θ_s is the mechanical angle in the airgap with respect to stator reference. The airgap flux density (B_g) produced by the interaction of the magnet MMF with the airgap permeance, considering only the DC and fundamental component of Λ, is given by [19]

$$\begin{aligned} B_g(\theta_s, t) &= B_{P_r} \cos(P_r\theta_s - \omega_e t) \\ &+ B_{Z-P_r} \cos\left[(Z - P_r)\theta_s + \omega_e t\right] \\ &+ B_{Z+P_r} \cos\left[(Z + P_r)\theta_s - \omega_e t\right] \end{aligned} \quad (3)$$

The resultant airgap flux density has a fundamental airgap flux density (B_{P_r}) and modulated airgap flux density components (B_{Z-P_r} and B_{Z+P_r}). The spectrum of the radial airgap flux density of the SPM-V machine in Fig. 1 with $Z = 6, P_r = 5, P_s = 1$ is shown in Fig. 2. The three airgap flux density coefficients in (3), i.e. B_{P_r}, B_{Z-P_r} and B_{Z+P_r} are also highlighted.

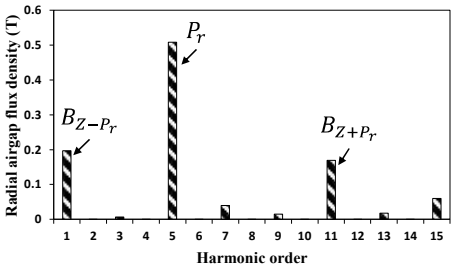

Fig. 2. Spectrum of open circuit radial airgap flux density for the SPM-V machine with $Z = 6, P_r = 5, P_s = 1$.

The modulated airgap flux density B_{z-P_r} is a subharmonic field which rotates at a mechanical speed $P_r/(Z - P_r)$ times faster than the fundamental airgap flux density. To utilize this modulated airgap flux density component and to maximize the torque capability in a SPM-V machine, the stator winding pole pair follows the rule [20]

$$P_s = Z - P_r \quad (4)$$

The ratio of the speed of modulated airgap field [$(Z - P_r)^{\text{th}}$] to the mechanical speed of the rotor is defined as the gear ratio of the SPM-V machine and is given by

$$G_r = \frac{P_r}{(Z - P_r)} = \frac{P_r}{P_s} \quad (5)$$

Since all the three flux densities in (3) generate the same electrical frequency, they all contribute to the induced EMF and thereby the average torque. The induced EMF (E_{ph-v}) can therefore be obtained by integrating the airgap flux density over one coil pitch as [19]

$$E_{ph-v} = \frac{k_w T_{ph} \omega_m D_g L_{stk}}{\sqrt{2}} \left(G_r B_{Z-P_r} + B_{P_r} + \frac{P_r}{(Z + P_r)} B_{Z+P_r} \right) \quad (6)$$

where k_w is the fundamental winding factor, T_{ph} is the number of series turns per phase, ω_m is the rotor mechanical angular velocity, D_g and L_{stk} are the airgap diameter and the stack length, respectively. The induced EMF can be further represented in terms of airgap permeance coefficients and gear ratio as (detailed derivation is given in APPENDIX)

$$E_{ph-v} = \frac{k_w T_{ph} \omega_m D_g L_{stk} B_{P_r}}{\sqrt{2}} \left(\frac{G_r^2}{(2G_r + 1)} \Lambda_r + 1 \right) \quad (7)$$

where Λ_r is the relative airgap permeance defined as the ratio of the fundamental component (Λ_1) to the DC component (Λ_0) of airgap permeance coefficient. For the study of induced EMF of the SPM-V machine compared to the conventional SPM (E_{ph-c}) machine for different airgap lengths, the per unit EMF (E_{PU}) term is introduced as

$$E_{PU} = \frac{E_{ph-v}}{E_{ph-c}} \quad (8)$$

For a SPM-V machine designed with the same machine parameters as the conventional SPM machine, E_{PU} is

$$E_{PU} = \left(\frac{G_r^2}{(2G_r + 1)} \Lambda_r + 1 \right) = K_{ver} + 1 \quad (9)$$

where $K_{ver} = \frac{G_r^2}{(2G_r+1)} \Lambda_r$, is the Vernier factor which is the extra EMF component generated in an SPM-V machine, which does not exist in a conventional SPM machine. From (9), it can be found that the induced EMF of SPM-V machine, for a given gear ratio (G_r), is largely a function of the relative airgap permeance (Λ_r). Moreover, for a given airgap length (as B_{P_r} is assumed the same for the two machines), the induced EMF of an SPM-V machine appears to be always greater than that of its conventional SPM counterpart. The above conclusion derived from (9) will be verified using 2D FEA analysis in the following sections.

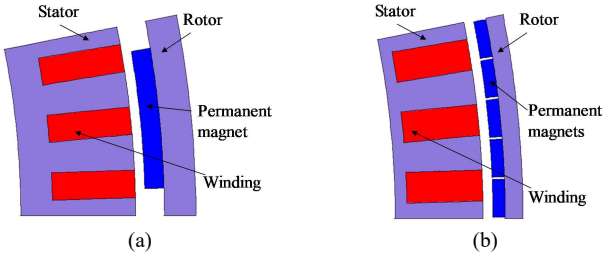

Fig. 3. Comparison of 2D models (one pole). (a) conventional SPM machine and (b) SPM-V machine.

III. 2D Finite Element Modelling

The 2D FEA model for one coil pitch of the conventional SPM machine with an outer rotor topology is shown in Fig. 3(a). The key parameters of the conventional SPM machine are given in TABLE I. The airgap length is varied from 1mm to 5mm with an incremental step of 1mm.

The SPM-V machine shown in Fig. 3(b) is derived from the conventional SPM machine by changing the slot/pole number which follows the rule given in (4). For each airgap length, the slot/pole number combination of the SPM-V machine is varied (with G_r=5) to evaluate the optimal performance. The different slot/pole number combinations used in this study for the SPM-V machine are given in TABLE II. All the designs for both the conventional SPM and SPM-V machines are globally optimized for achieving the maximum torque capability. It is worth noting that during the optimization process, all the dimensions shown TABLE I are maintained the same for the two machines when they have different airgap lengths. This will inevitably lead to different output powers as will be investigated in the following sections. However, for having the same thermal performance between the two machines, the copper loss has been kept the same.

TABLE I KEY PARAMETERS OF SPM MACHINE

Rated power (kW)	3	Magnet volume (m^3)	0.000408
Rated speed (rpm)	170	Magnet B_r, μ_r	1.23,1.02
Rotor outer diameter (mm)	426.4	Phase current (Arms)	2.5
Airgap length (mm)	1,2,3,4,5	Turns/phase	720
Stack length (mm)	110		

TABLE II SLOT/POLE NUMBER COMBINATIONS

Machine type	Z	P_r	P_s	LCM (Z, $2P_r$)
Conventional	96	16	16	96
Vernier	36	30	6	180
Vernier	48	40	8	240
Vernier	72	60	12	360
Vernier	96	80	16	480
Vernier	120	100	20	600

Note: LCM is the least common multiple.

IV. Comparison for Different Airgap Lengths

A. Induced EMF

According to (9), for a given gear ratio G_r, the per unit induced EMF (E_{PU}) is directly proportional to Λ_r. The value of Λ_r computed using 2D FEA [21] for different airgap lengths across different slot/pole numbers for the SPM-V machine is shown in Fig. 4(a). It can be observed that for a given slot/pole number, Λ_r decreases with increase in airgap length. Similarly, for a given airgap length, Λ_r decreases with increase in pole number. E_{PU} calculated using (9) as shown in Fig. 4(b) follows the same trend as Λ_r. The SPM-V machine shows significantly higher induced EMF (2.15 times) than its conventional SPM counterpart towards smaller airgap length and lower slot/pole numbers. With the increase in airgap length, the extra EMF gained over conventional SPM machine with a similar airgap length diminishes. However, the SPM-V machine always exhibits a higher EMF capability compared to the conventional SPM machine according to (9).

The induced EMF predicted directly using 2D FEA is shown in Fig. 5. Unlike the results predicted by (9), 2D FEA results show that the induced EMF for an SPM-V machine can be lower than the conventional SPM machine with the same airgap length. Moreover, the maximum gain in the EMF (1.62 times) achievable for the SPM-V machine predicted by 2D FEA is much lower than that predicted by (9). For very small airgap length, the SPM-V machine generally outperforms the conventional SPM machine for the wide range of slot/pole numbers considered. However, with increase in airgap length, the choice of slot/pole numbers for SPM-V machine which can achieve higher EMF than the conventional SPM counterpart is limited.

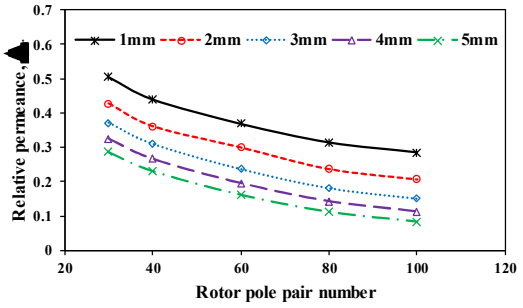

(a)

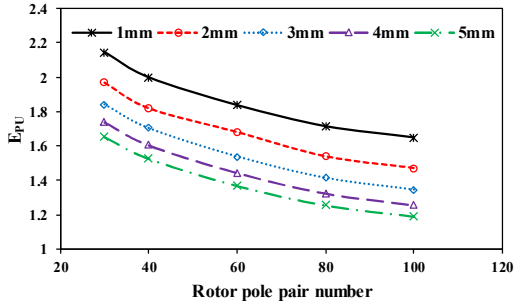

(b)

Fig. 4. Comparison of (a) Λ_r predicted using 2D FEA [21] and (b) E_{PU} calculated using (9) for different airgap lengths across all slot/pole numbers of SPM-V machine.

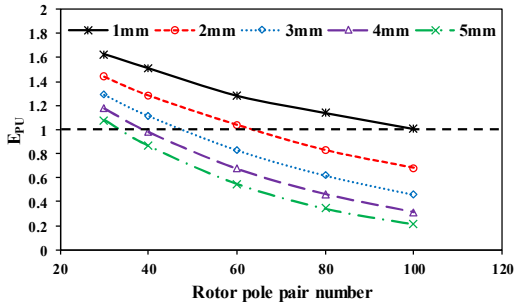

Fig. 5. Comparison of E_{PU} predicted directly using 2D FEA for different airgap lengths across all slot/pole numbers of SPM-V machine.

The main reason for the deviation between the results of 2D FEA and (9) is mainly due to the assumption that the fundamental airgap flux density (B_{P_r}) between the two machines is the same for a given airgap length. For the comparison of fundamental airgap flux density, the per unit value (B_{P_r-PU}) is introduced as

$$B_{P_r-PU} = \frac{B_{P_r-v}}{B_{P_r-c}} \quad (10)$$

where B_{P_r-v} and B_{P_r-c} are the fundamental airgap flux density of the SPM-V machine and the conventional SPM machine respectively for the same airgap length. The comparison of B_{P_r-PU} predicted by 2D FEA for different airgap lengths across all the slot/pole number of SPM-V machine is shown in Fig. 6.

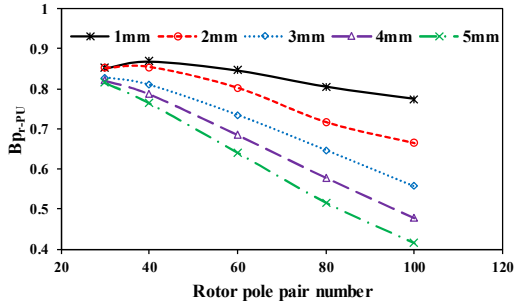

Fig. 6. Comparison of B_{P_r-PU} predicted directly using 2D FEA for different airgap lengths across all slot/pole numbers of SPM-V machine.

It can be observed that B_{P_r-v} is always lower than the B_{P_r-c} with the same airgap length. The maximum value of B_{P_r-PU} is about 0.87 at 1mm airgap length for very low slot/pole number. This value can decrease significantly to a minimum of 0.41 at 5mm airgap length towards high slot/pole number. This is largely due to high inter-pole leakage flux leading to reduced flux per pole for the SPM-V machine with large pole pair. The comparison of open circuit flux distribution at 5mm airgap length between the conventional SPM machine with $N_s = 96, P_r = 16$ and the SPM-V machine with $N_s = 96, P_r = 80, P_s = 16$ over one coil pitch is shown in Fig. 7.

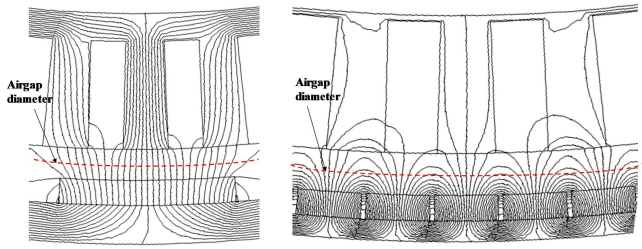

Fig. 7. Comparison of open-circuit flux distributions over one coil pitch at an airgap length of 5mm. (a) conventional SPM machine with $N_s = 96, P_r = 16$ and (b) SPM-V machine with $N_s = 96, P_r = 80, P_s = 16$.

Even at an airgap length of 5mm, the inter-pole leakage flux for the conventional SPM machine is negligible compared to the flux per pole. However, for the SPM-V machine, almost all the fluxes generated by the 5 magnets under one coil pitch can be regarded as leakage fluxes. This results in much lower E_{PU} for the SPM-V machine towards 5mm airgap length as shown in Fig. 5. Therefore, the assumption of the same fundamental airgap flux density (B_{P_r}) in (9) between the two machines for the same airgap length is not acceptable especially towards large slot/pole numbers.

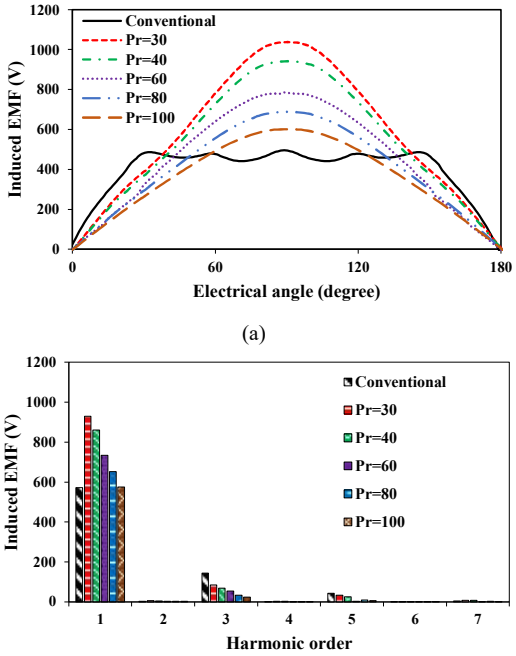

Fig. 8. Comparison of induced EMF (a) waveforms and (b) spectra at 1mm airgap length between conventional SPM and SPM-V machines with different slot/pole number combinations.

The comparison of induced EMF waveform between conventional SPM and SPM-V machine at 1mm airgap length is shown in Fig. 8 (a). The corresponding harmonic spectra shown in Fig. 8 (b) reveal that the conventional SPM machine has significantly larger amount of harmonics compared to the SPM-V machine. This means that the SPM-V machine achieves a much better voltage quality with nearly sinusoidal EMF wave shape.

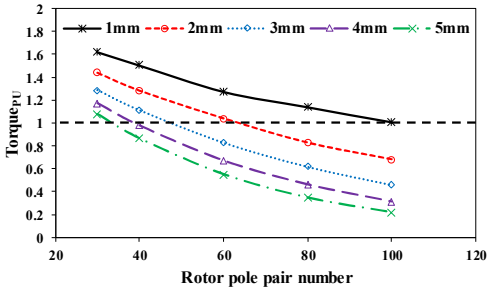

Fig. 9. Comparison of $Torque_{PU}$ predicted directly using 2D FEA for different airgap lengths across all slot/pole numbers of the SPM-V machine.

B. Average Torque and Torque Ripple

As mentioned in section III, the phase current is maintained the same for different airgap lengths across all slot/pole numbers of SPM-V machine. Therefore, the torque performance is expected to largely follow the induced EMF trend unless the machine has reached magnetic saturation. Similar to induced EMF, the per unit torque ($Torque_{PU}$) is introduced to compare the performance of SPM-V machine with conventional SPM machine. The $Torque_{PU}$ comparison for different airgap lengths across all slot/pole numbers of SPM-V machine is shown in Fig. 9. The torque performance is very much similar to the induced EMF as the impact of saturation is not significant.

For making the study more generic and useful for the SPM-V machine design, the slot/pole number with different airgap lengths is represented as normalized pole pitch ($\overline{\tau_r}$) defined as

$$\overline{\tau_r} = \frac{\tau_r}{g + \frac{h_m}{\mu_{rec}}} \tag{11}$$

where τ_r is the rotor pole pitch, g is the mechanical airgap length, h_m and μ_{rec} are the magnet thickness and recoil permeability.

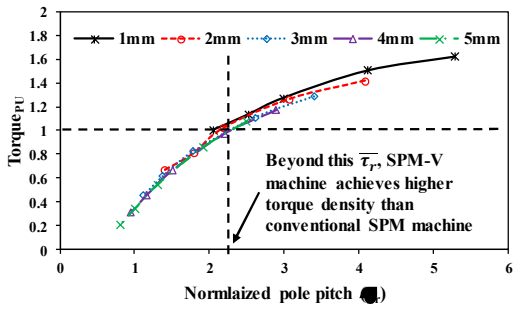

Fig. 10. Comparison of $Torque_{PU}$ predicted directly using 2D FEA as a function of normalized pole pitch ($\overline{\tau_r}$) of the SPM-V machine.

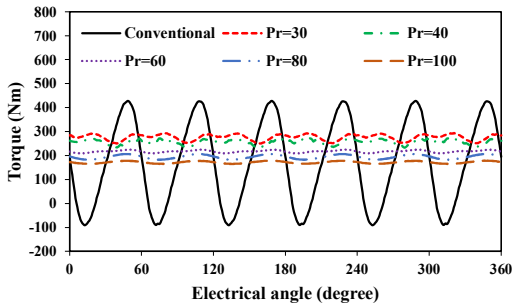

(a)

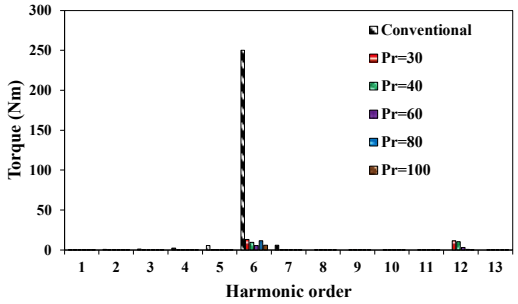

(b)

Fig. 11. Comparison of torque (a) waveforms and (b) spectra at 1mm airgap length between conventional SPM and SPM-V machines with different slot/pole number combinations.

$Torque_{PU}$ as a function of $\overline{\tau_r}$ is shown in Fig. 10. It can be observed that $Torque_{PU}$ is clearly a function of $\overline{\tau_r}$ with all the torque curves merging into a single curve. The study shows that for a 3kW power rating, the SPM-V machine designed around a $\overline{\tau_r}$ >2.2 can achieve higher torque density than the conventional counterpart. The torque waveforms and their spectra for 1mm airgap length are shown in Fig. 11. It can be observed that the torque ripple of the conventional SPM machine is significantly high. This is largely due to the 6th order cogging torque harmonic. On the contrary, with nearly sinusoidal phase EMF and negligible cogging torque, the SPM-V machine produces very low ripple. The reason for SPM-V machine's low cogging torque can be explained as follows.

For generating high torque, the SPM-V machine generally relies on higher gear ratio. This makes the number of stator slots very close to the rotor pole pair number as given by (4) and (5). Therefore, the Least Common Multiple (LCM) between N_s and $2P_r$ for the SPM-V machine is in general higher than that of the conventional SPM machine. It is generally true that the higher the value of LCM, the lower the cogging torque [22].

The comparison of the cogging torque [$(CT_{max}$-$CT_{min})/T_{av}\times100\%$, where CT_{max}, CT_{min} are the maximum, the minimum values of cogging torque and T_{av} is the average on-load torque during one electrical period] for different airgap lengths across all slot/pole numbers of the SPM-V machine is shown in Fig. 12(a). Whereas the cogging torques for the conventional SPM machine are given in TABLE III.

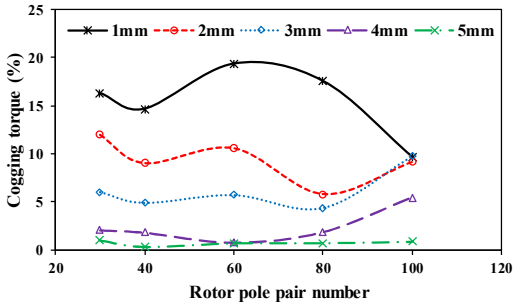

(a)

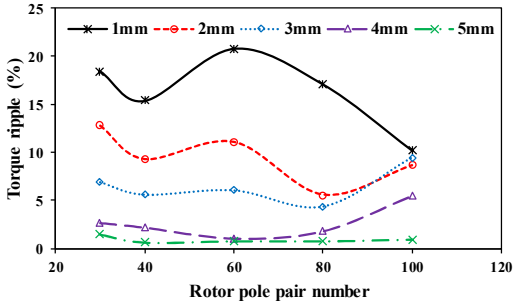

(b)

Fig. 12. Comparison of (a) cogging torque and (b) torque ripple for different airgap lengths across all slot/pole numbers of SPM-V machine.

TABLE III COGGING TORQUE AND TORQUE RIPPLE VALUES FOR CONVENTIONAL SPM MACHINE

Parameter	Airgap length(mm)				
	1	2	3	4	5
Cogging torque (%)	304	165.8	69	5.3	29
Torque ripple (%)	305	166.5	69	9.6	30

For the same airgap length, the conventional SPM machine has low LCM, as highlighted in TABLE II, and significantly higher cogging torque compared to the SPM-V machine. In general, for conventional SPM machine with integer slot winding (slots/pole/phase=1), different cogging torque reduction techniques such as magnet shaping, skewing, etc. can be adopted. However, for this analysis, these techniques

are not incorporated in the model to have a fair comparison with the SPM-V machine. Moreover, since the global optimization was performed for maximizing the torque performance, the cogging torque may not be optimal and is found to be more than reasonable values for conventional SPM. This is one of the reasons why the instantaneous torque of the conventional SPM machine can be negative for 1mm airgap length, as shown in Fig. 11(a). As can be expected, cogging torque is found to be decreasing with the increase of airgap length for both the machines. However for a given airgap length, there is no specific trend observed across slot/pole numbers of the SPM-V machine.

The on-load torque ripples [$(T_{max}$-$T_{min})/T_{av}\times100\%$, where T_{max} and T_{min} are the maximum and the minimum values of on-load torque during one electrical period] for different airgap lengths across all slot/pole numbers of the SPM-V machine are shown in Fig. 12(b). It is observed that for both machines, torque ripples are largely determined by the cogging torque.

C. Power Factor

Vernier machines are known for their relatively poor power factor compared to conventional PM machines [23], [24]. The comparison of power factors (at rated load) for different airgap lengths across all slot/pole numbers of the SPM-V machine is shown in Fig. 13. The power factors for the conventional SPM machine are found to be almost unity for all the airgap lengths. However, for the SPM-V machine, there is a significant drop in power factor with increase in airgap length, especially for higher pole numbers. The maximum power factor achievable for the SPM-V machine is 0.97 at 1mm airgap length and the minimum value is 0.51 at 5mm airgap length. This drop in power factor for the SPM-V machine is due to high inter-pole leakage at high slot/pole numbers as shown in Fig. 7(b).

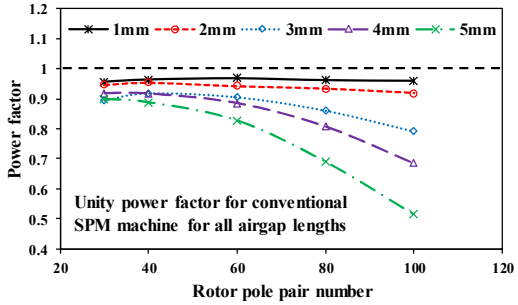

Fig. 13. Comparison of power factor predicted directly using 2D FEA for different airgap lengths across all slot/pole numbers of the SPM-V machine.

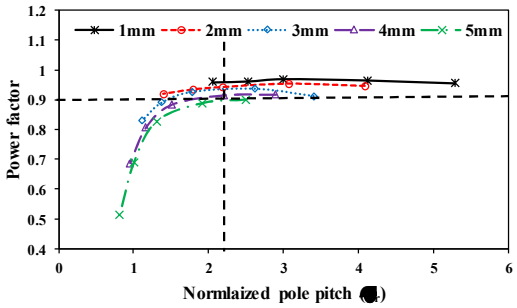

Fig. 14. Comparison of power factor predicted directly using 2D FEA as a function of ($\overline{\tau_r}$) of the SPM-V machine.

The power factor as a function of $\overline{\tau_r}$ shown in Fig. 14 reveals that a value greater than 0.9 is achievable with $\overline{\tau_r}$ >2.2 at 3kW power level.

V. Conclusion

The performance comparison between the SPM-V machine and the conventional SPM machine for different airgap lengths is investigated. The study shows that the SPM-V machine outperforms the conventional SPM machine for small airgap lengths (at 3kW power level) with significantly higher torque density, lower torque ripple and comparable power factor. However, the conventional SPM machine is definitely emerging as a better choice for designs with larger airgap length ($\overline{\tau_r}$ <2.2).

VI. Appendix

The fundamental (B_{P_r}) and the modulated airgap flux densities (B_{Z-P_r} and B_{Z-P_r}) can be presented in terms coefficients of airgap permeance as [19], [20]

$$B_{P_r} = F_1\Lambda_0$$
$$B_{Z-P_r} = B_{Z+P_r} = \frac{1}{2}F_1\Lambda_1 \quad (12)$$

Substituting (12) in (6) we get

$$E_{ph-v} = \frac{k_w T_{ph}\omega_m D_g L_{stk} B_{P_r}}{\sqrt{2}}\left[\frac{\Lambda_r}{2}\left(G_r + \frac{P_r}{(Z+P_r)}\right)+1\right] \quad (13)$$

Combining (4) and (5) we get

$$Z = (G_r + 1)P_s \quad (14)$$

Substituting (5) and (14) in (13) we get

$$E_{ph-v} = \frac{k_w T_{ph}\omega_m D_g L_{stk} B_{P_r}}{\sqrt{2}}\left(\frac{G_r^2}{(2G_r+1)}\Lambda_r + 1\right) \quad (15)$$

References

[1] Y. Yuan, W. Meng, X. Sun, and L. Zhang, 'Design optimization and analysis of an outer-rotor direct-drive permanent-magnet motor for medium-speed electric vehicle', *World Electr. Veh. J*, vol. 10, p. 16, 2019.

[2] F. Jin, J. Si, Z. Cheng, P. Su, L. Dong, and G. Qi, 'Analysis of a six-phase direct-drive permanent magnet synchronous motor with novel toroidal windings', in *2019 IEEE Veh. Pow. and Prop. Conf. (VPPC)*, pp. 1–6, 2019.

[3] W. Gul, Q. Gao, and W. Lenwari, 'Optimal design of a 5-MW double-stator single-rotor PMSG for offshore direct drive wind turbines', *IEEE Trans. Ind. Appl.*, vol. 56, no. 1, pp. 216–225, Jan. 2020.

[4] Y. Guan, Z. Q. Zhu, Z. Azar, A. S. Thomas, F. Vedreno-Santos, G.. J. Li, M. Odavic, 'Comparison of electromagnetic performance of 10-MW superconducting generators with different topologies for offshore direct-drive wind turbines', *IEEE Trans. Appl. Supercond.*, vol. 27, no. 7, pp. 1–11, Oct. 2017.

[5] T. M. Jahns, 'The expanding role of PM machines in direct-drive applications', in *2011 Int. Conf. Electrical Machines and Systems,* pp. 1–6, 2011.

[6] Y. Feng, F. Li, S. Huang, and N. Yang, 'Variable-flux outer-rotor permanent magnet synchronous motor for in-wheel direct-drive applications', *Chinese J. Electr. Eng.*, vol. 4, no. 1, pp. 28–35, Mar. 2018.

[7] C. Yicheng, P. Pillay, and A. Khan, 'PM wind generator topologies', *IEEE Trans. Ind. Appl.*, vol. 41, no. 6, pp. 1619–1626, Nov/Dec. 2005.
[8] Z. Zhang, A. Chen, A. Matveev, R. Nilssen, and A. Nysveen, 'High-power generators for offshore wind turbines', *Energy Procedia*, vol. 35, pp. 52–61, Jan. 2013.
[9] D. Bang, H. Polinder, G. S. Shrestha, and J. A. Ferreira, "Review of generator systems for direct-drive wind turbines," in *European Wind Energy Conference & Exhibition*, *Belgium*, vol. 31, pp. 1–11, 2008.
[10] Z. Q. Zhang, A. Matveev, R. Nilssen, and A. Nysveen, 'Ironless permanent-magnet generators for offshore wind turbines', *IEEE Trans. Ind. Appl.*, vol. 50, no. 3, pp. 1835–1846, May 2014.
[11] W. Zhang, M. Lin, D. Xu, X. Fu, and L. Hao, 'Novel fault-tolerant design of axial field flux-switching permanent magnet machine', *IEEE Trans. Appl. Supercond*, vol. 24, no. 3, pp. 1–4, Jun. 2014.
[12] B. McGilton, M. Mueller, and A. McDonald, 'Review of magnetic gear technologies and their applications in marine energy', *Proc. of the 5th IET Int. Conf. on Renewable Power Generation (RPG) 2016*, pp. 1–6, 2016.
[13] L. Jian, K. T. Chau, and J. Z. Jiang, "A magnetic-geared outer-rotor permanent-magnet brushless machine for wind power generation," *IEEE Trans. Ind. Appl.*, vol. 45, no. 3, pp. 954–962, May 2009.
[14] J. Li, K. T. Chau, J. Z. Jiang, C. Liu, and W. Li, "A new efficient permanent-magnet Vernier machine for wind power generation," *IEEE Trans. Magn.*, vol. 46, no. 6, pp. 1475–1478, Jun. 2010.
[15] D. K. Jang and J. H. Chang, 'Design of a Vernier machine with PM on both sides of rotor and stator', *IEEE Trans. Magn.*, vol. 50, no. 2, Feb. 2014.
[16] Y. T. Gao, R. H. Qu, D. W. Li, and F. X. Chen, 'Force ripple minimization of a linear Vernier permanent magnet machine for direct-drive servo applications', *IEEE Trans. Magn.,* vol. 53, no. 6, Jun. 2017.
[17] S. Hyoseok, N. Niguchi, and K. Hirata, "Characteristic analysis of surface permanent-magnet Vernier motor according to pole ratio and winding pole number," *IEEE Trans. Magn.*, vol. 53, no. 11, pp. 1–4, Nov. 2017.
[18] D. W. Li, R. H. Qu, J. Li, L. Y. Xiao, L. L. Wu, and W. Xu, "Analysis of torque capability and quality in Vernier permanent-magnet machines," *IEEE Trans. Ind. Appl.*, vol. 52, no. 1, pp. 125–135, Jan. 2016.
[19] L. Wu, R. Qu, D. Li, and Y. Gao, "Influence of pole ratio and winding pole numbers on performance and optimal design parameters of surface permanent-magnet Vernier machines," *IEEE Trans. Ind. Appl.*, vol. 51, no. 5, pp. 3707–3715, Sep. 2015.
[20] A. Toba and T. A. Lipo, "Generic torque- maximizing design methodology of surface permanent- magnet Vernier machine," *IEEE Trans. Ind. Appl.*, vol. 36, no. 6, pp. 1539–1546, Nov. 2000.
[21] L. R. Huang, J. H. Feng, S. Y. Guo, J. X. Shi, W. Q. Chu, and Z. Q. Zhu, "Analysis of torque production in variable flux reluctance machines," *IEEE Trans. Energy Convers.*, vol. 32, no. 4, pp. 1297–1308, Dec. 2017.
[22] Z. Q. Zhu and D. Howe, 'Influence of design parameters on cogging torque in permanent magnet machines', *IEEE Trans. Energy. Convers.*, vol. 15, no. 4, pp. 407–412, Dec. 2000.
[23] Y. Oner, Z. Q. Zhu, and W. Chu, "Comparative study of Vernier and interior PM machines for automotive application," *Proc. IEEE Vehicle Power and Propulsion Conf.*, Hangzhou, China, Oct. 2016, pp. 1-6.
[24] Z. S. Du and T. A. Lipo, "Torque performance comparison between a ferrite magnet Vernier motor and an industrial interior permanent magnet machine," *IEEE Trans. Ind. Appl.*, vol. 53, no. 3, pp. 2088–2097, May 2017.

VII. BIOGRAPHIES

D. K. Kana Padinharu received his B.Tech. in electrical and electronics engineering from College of Engineering Trivandrum, Kerala, India in 2004 and MSc.(Engg.) in high voltage engineering from Indian Institute of Science Bangalore, India in 2007. He worked for General Electric Company in India from 2007 to 2017, where he was involved in designing high power synchronous generators. Currently, he is pursuing Ph.D. in electrical engineering from the University of Sheffield, U.K. His research interests are mainly focused on design, modelling and optimization of permanent magnet machines.

G. J. Li received his BEng, MSc and PhD degrees in electrical and electronic engineering from the Wuhan University, China, in 2007, University of Paris XI, France, in 2008, and the Ecole Normale Supérieure (ENS) de Cachan, Paris, France, in 2011, respectively. He joined the University of Sheffield in June 2012 as a post-doctoral research associate at EMD Group. In September 2013, he took up a Lectureship in Electrical Machines within the EMD Group at the University of Sheffield, where he is currently an Associate Professor. His main research interests include the design, fault analysis and thermal management of electrical machines for renewable energy, automotive, more electrical aircraft, etc.

Z. Q. Zhu has been with the University of Sheffield since 1988, where he currently holds the Royal Academy of Engineering/Siemens Research Chair and is the Head of the Electrical Machines and Drives Research Group. His current major research interests include the design and control of permanent magnet brushless machines and drives for applications ranging from automotive through domestic appliances to renewable energy. He is a fellow of IEEE, IET and the Royal Academy of Engineering.

Ziad Azar received the B.Eng. degree in electrical engineering from the University of Damascus, Damascus, Syria, in 2003 and the M.Sc. degree in electronic and electrical engineering and the Ph.D. degree in electrical engineering from The University of Sheffield, Sheffield, U.K., in 2008 and 2012, respectively. His major research interests during his Ph.D. studies included the modelling, design, and analysis of permanent-magnet and magnetless brushless machines for automotive applications. In 2012, he joined Siemens Games Renewable Energy, where he is currently the generator team manager in the technology development department, focus has been on maturing and developing of new technologies for direct-drive wind power generator.

A. Thomas received the M.Eng. and Ph.D. degrees in electronic and electrical engineering from the University of Sheffield, Sheffield, U.K., in 2005, and 2009, respectively. He is currently with the Sheffield Siemens Gamesa Renewable Research Centre, University of Sheffield. His research focuses on the modeling, design and analysis of permanent-magnet brushless machines.

R. Clark obtained his B.Eng. degree in Electrical Engineering from the University of Sheffield and received a Ph.D. in 1999 for research on permanent magnet actuators. Following several years as a post-doctoral Research Associate, he was awarded a 5 year Royal Academy of Engineering Research Fellowship and became a Lecturer in Electrical Engineering at the University of Sheffield in 2005. In 2007, he joined Magnomatics, a University of Sheffield spin-out company developing novel electrical motors and generators and magnetic transmissions, where he held posts of R&D Manager, Research Director and Principal Engineer. He joined Siemens Gamesa Renewable Energy as Electromagnetic Specialist in October 2017.